Research Article Vol. 8, No. 11 / November 2021 / Optica 1501

Fabrication of freeform optical components by fluidic shaping

Mor Elgarisi,[1,†] Valeri Frumkin,[1,†] Omer Luria,[1] and Moran Bercovici[1,*]

[1]Faculty of Mechanical Engineering, Technion–Israel Institute of Technology, Technion City, Haifa 3200003, Israel
*Corresponding author: mberco@technion.ac.il

Received 26 July 2021; revised 27 September 2021; accepted 29 September 2021 (Doc. ID 438763); published 18 November 2021

Freeform optical components enable advanced manipulation of light that is not possible with traditional optical systems. However, their fabrication relies on machining processes that are complex, time-consuming, and require significant infrastructure. Here we present the ability to shape liquid volumes and solidify them into desired freeform components, enabling rapid prototyping of freeform components with high surface quality. The method is based on controlling the minimum energy state of the interface between a curable optical liquid and an immersion liquid, by dictating a geometrical boundary constraint. We provide an analytical solution for the resulting topography given a predefined boundary and demonstrate the fabrication of freeform components with sub-nanometer surface roughness within minutes. Such a fabrication capability, that allows for rapid prototyping of high-quality components, has the potential to answer an unmet need in the optical design industry—allowing researchers and engineers to rapidly test freeform design concepts. It can be further envisioned to be expanded to an industrial scale, allowing for mold-less fabrication of freeform optics.

https://doi.org/10.1364/OPTICA.438763

1. INTRODUCTION

Freeform optics is a broad term that refers to any optical component, reflective or refractive, in which one or more of its optical surfaces perform complex phase manipulation on the incoming wavefront, beyond that achievable using traditional optical components. A single freeform optical component can replace the functionality of multiple traditional lenses (spherical or aspherical) within an optical system, allowing significant reduction in dimensions and assembly complexity. Moreover, freeform surfaces can provide new functionality that is not attainable using standard optics [1–6].

In recent years, the advent in computer-based optical design enabled the simulation of complex components and led to tremendous growth in the use of freeform optics for new applications [7]. These include multifocal corrective eyewear [8,9], telescopes [10–12], beam shaping [13], ultra-short projection lenses [14,15], panoramic imaging [16], solar energy concentration [17], and photolithography [18].

Small freeform components can be fabricated by using microstructuring techniques such as micromachining, lithography, and etching [19,20]. Yet these methods are limited to characteristic scales of up to tens of micrometers in depth, and up to several mm^2 in area [20]. The fabrication of larger components relies on machining approaches such as grinding, milling, and turning, followed by polishing or finishing [7,21–24]—processes that remain complex, expensive, and time-consuming. Additive manufacturing is a natural candidate when seeking to construct arbitrary three-dimensional configurations. However, existing 3D printing technologies are primarily based on layer-by-layer fabrication and cannot yet provide the required surface quality for optical applications. Better surface quality can be obtained using post-printing processes such as reflow or coatings [25–28], but at the cost of additional complexity, fabrication time, and reduced control over the precise shape of the surface. Furthermore, since printing time is proportional to the volume of the object (in contrast to mechanical processing that is roughly proportional to the surface area), practical considerations limit the fabrication to small lenses [25–28]. An additive manufacturing method that enables us to achieve smooth optical surfaces was demonstrated by two-photon polymerization, yet this method is also limited to the scale of micrometers [29,30].

Recently, work by Frumkin and Bercovici suggested a new method of fabricating optical components based on shaping of liquid volumes [31]. Their method is based on injection of a curable optical fluid into a rigid bounding frame contained within an immiscible immersion liquid environment. The authors showed that using a simple cylindrical frame, the balance between gravitational forces, hydrostatic forces, and surface tension forces, enables the creation of spherical and aspherical lenses. The method was shown to be scale-invariant, allowing the production of lenses at any size while maintaining a surface roughness of 1 nm, without the need for any further mechanical processes. Furthermore, the production time only weakly depends on the size of the produced lens.

In this work, we introduce an extension of this scale-invariant fluidic shaping method to non-axisymmetric boundary conditions, allowing for rapid fabrication of freeform optical components. We study the case of a cylindrical bounding frame

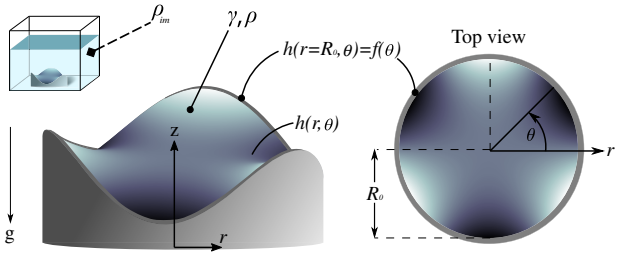

Fig. 1. Schematic illustration of the examined configuration. An optical liquid of density ρ wets the inner surface of a cylindrical frame of radius R_0 that is entirely submerged within an immiscible liquid of density ρ_{im}. The surface tension between the liquids is γ. The resulting surface shape $h(r,\theta)$ is determined by a balance between gravity, hydrostatic pressure, and surface tension, subjected to the prescribed boundary condition $h(R_0,\theta)=f(\theta)$ and the total volume V of the injected liquid.

whose height varies azimuthally, and based on free-energy minimization, derive an analytical model that relates the shape of this bounding frame to that of the enclosed liquid interface forming the freeform surface. These boundary conditions, which can be represented as a sum of azimuthal waves, together with the injected volume and effective buoyancy, provide an infinite number of degrees of freedom which translate into a family of freeform surfaces. These can be naturally represented by a sum of polar–Bessel functions in a similar manner to the commonly used Zernike polynomials [32]. Using bounding frames created with a standard 3D printer, we demonstrate the ease of fabrication of several freeform components. We use frames defined by a single wavenumber to demonstrate common freeform surfaces such as saddles, tilts (bifocal), and quatrefoils, as well as frames defined by superposition of waves yielding arbitrary desired surfaces. All those components enjoy a surface quality of the order of 1 nm, characteristic of the fluidic shaping method, without the need for any subsequent polishing steps.

2. THEORY

We consider a configuration similar to that described in Fig. 1, where an optical liquid of density ρ and volume V is injected into a cylindrical bounding surface of radius R_0 and height $h(R_0,\theta)=f(\theta)$. The liquid is suspended in an immersion liquid of density ρ_{im}, resulting in an effective density of $\Delta\rho=\rho-\rho_{im}$.

We assume that the liquid wets the inner walls of the frame and forms an interface $h(r,\theta)$ with the immersion liquid. The shape of that interface is determined by a balance between surface tension, hydrostatic forces, and gravitational forces. The relative importance of the body force to surface forces can be expressed by the dimensionless Bond number, $Bo=\frac{R_0^2}{\ell_c^2}=\frac{|\Delta\rho|g\,R_0^2}{\gamma}$, where $\ell_c=\sqrt{\frac{\gamma}{|\Delta\rho|g}}$ is the capillary length, γ is the interfacial energy between the two liquids, and g is Earth's gravity directed in the negative $\hat{z}$ direction.

At the steady state, the fluidic interface $h(r,\theta)$ will take a shape that minimizes the free energy of the system under a fixed volume constraint. The free energy functional, Π, is given by

$$\Pi=\int_0^{2\pi}\int_0^{R_0}F(r,\theta)\mathrm{d}r\,\mathrm{d}\theta;\quad F(r,\theta)$$
$$=\left(\gamma\sqrt{1+\left(\frac{dh}{dr}\right)^2+\frac{1}{r^2}\left(\frac{dh}{d\theta}\right)^2}+\frac{1}{2}\Delta\rho g h^2+\lambda h\right)r \quad (1)$$

and is composed of two contributions: the surface energy associated with the interface between the liquids, and the gravitational potential energy that includes Earth's gravity and the hydrostatic buoyancy force. The last term in $F(r,\theta)$ represents the volume constraint, with λ being a Lagrange multiplier.

At equilibrium, the first variation of the energy functional vanishes, i.e., $\delta\Pi=0$, yielding the standard Euler–Lagrange equation [33],

$$\frac{\partial F}{\partial h}-\frac{d}{dr}\frac{\partial F}{\partial h_r}-\frac{d}{d\theta}\frac{\partial F}{\partial h_\theta}=0. \quad (2)$$

We define the following dimensionless variables:

$$R=\frac{r}{R_0},\quad \Theta=\theta,\quad H(R,\Theta)=\frac{h(R,\Theta)-h_0}{d_c},$$
$$P=\left(\frac{\lambda}{|\Delta\rho|\,g\,d_c}-\frac{h_0}{d_c}\right),\quad Bo=\frac{|\Delta\rho|\,g\,R_0^2}{\gamma},\quad \varepsilon=\left(\frac{d_c}{R_0}\right)^2, \quad (3)$$

where h_0 is the average height of the bounding frame $\left(h_0=\frac{\int_0^{2\pi}f(\theta)\mathrm{d}\theta}{2\pi}\right)$ and d_c is the characteristic deformation of the surface relative to the frame, yielding the explicit dimensionless form of Eq. (2),

$$(-H+P)\,Bo\,R^2-\frac{H_{RR}\left(R^2+\varepsilon H_\Theta^2\right)+\left(RH_R+H_{\Theta\Theta}\right)\left(1+\varepsilon H_R^2\right)-2\varepsilon H_\Theta H_R H_{R\Theta}+\frac{2}{R}\varepsilon H_R H_\Theta^2}{\left(1+\varepsilon H_R^2+\frac{\varepsilon}{R^2}H_\Theta^2\right)^{3/2}}=0, \quad (4)$$

where H_R and H_Θ are the partial derivatives of $H(R,\Theta)$ with respect to R and Θ.

For most optical elements the characteristic deformation length d_c is significantly smaller than the component's radius, thus $\varepsilon=(\frac{d_c}{R_0})^2\ll 1$. Therefore, at the leading order in ε, and by defining $x=R\sqrt{Bo}$ and $\tilde{H}=H-P$, Eq. (4) reduces to the Helmholtz equation, $\tilde{H}x^2+x^2\tilde{H}_{xx}+x\tilde{H}_x+\tilde{H}_{\Theta\Theta}=0$, the general solution to which is given by [34]

$$\tilde{H}(x,\theta)=\sum_{n=0}^{\infty}A_nJ_n(x)\cos(n\Theta)+\sum_{n=1}^{\infty}B_nJ_n(x)\sin(n\Theta). \quad (5)$$

Expressing the bounding surface height as a Fourier expansion, $f(\Theta)=a_0+\sum_{n=1}^{\infty}a_n\cos n\Theta+\sum_{n=1}^{\infty}b_n\sin n\Theta$, the mean average of the bounding height is $h_0=a_0$, and the constants A_n and B_n can be obtained by requiring Eq. (5) to satisfy the boundary condition $\tilde{H}(\sqrt{Bo},\Theta)=\frac{f(\Theta)-a_0}{d_c}-P$, yielding

$$H(x,\Theta)=P\left(1-\frac{J_0(x)}{J_0\left(\sqrt{Bo}\right)}\right)+\sum_{n=1}^{\infty}\frac{a_n/d_c}{J_n\left(\sqrt{Bo}\right)}J_n(x)\cos(n\Theta)$$
$$+\sum_{n=1}^{\infty}\frac{b_n/d_c}{J_n\left(\sqrt{Bo}\right)}J_n(x)\sin(n\Theta). \quad (6)$$

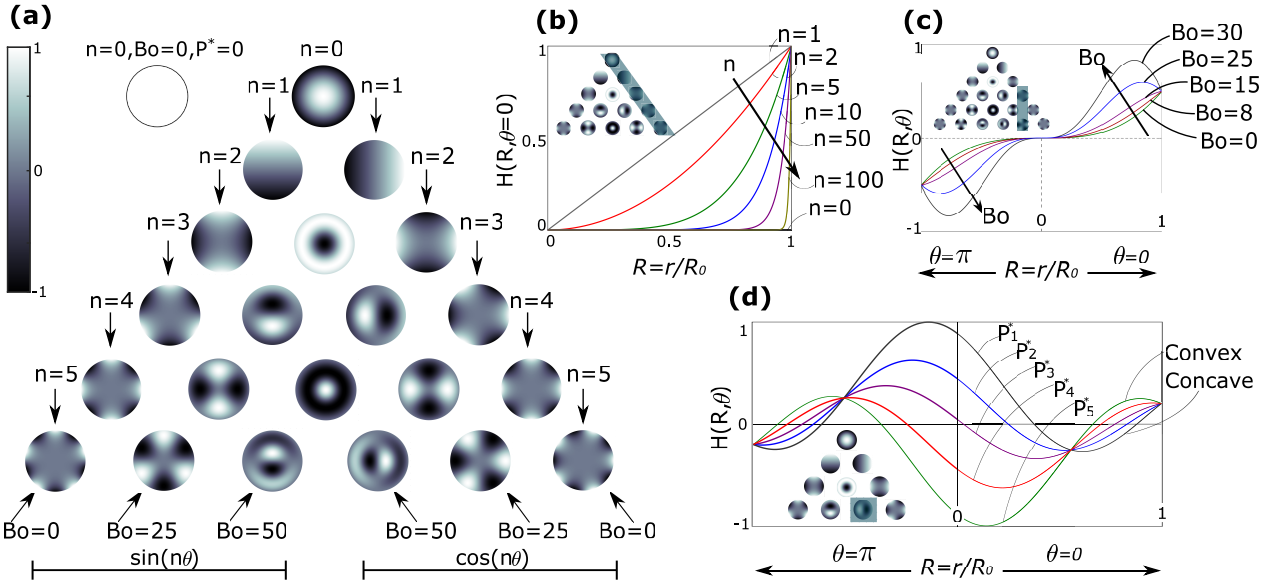

Fig. 2. Analytical results demonstrating the range of surfaces obtained by modification of the boundary conditions and the Bo number. (a) Normalized topography maps obtained for a range of Bo numbers and for periodic boundary conditions (columns) of the type $\sin(n\theta)$ (left side) and $\cos(n\theta)$ (right side). Each column corresponds to a different wavenumber n, and each layer in the pyramid corresponds to a different Bond number. For completeness, the trivial case of $h=0$, obtained for $n=0$, $Bo=0$ and $V=\pi R_0^2 a_0$ (i.e. $P^*=0$) is presented outside of the pyramid. (b) A radial cross section along $\theta=0$ for $Bo=0$, showing that an increase in the boundary's wavenumber, n, leads to faster decay of the amplitude toward the center, in accordance with Eq. (7). (c) A radial cross section along $\theta=0$ and $\theta=\pi$ for a fixed frame shape, $n=3$, showing that increasing the Bo number produces an inflection point in the surface and shifts the maxima from the boundary inward. (d) A radial cross section along $\theta=0$ and $\theta=\pi$ for a fixed frame shape, $n=1$ and a fixed Bond number, $Bo=25$, for different P values representing different volumes, $V_{P1}>V_{P2}>\dots V_{P5}$. The change in volume not only affects the magnitude of the topography but can also invert the local curvature.

In dimensional form, the solution is given by

$$h(r,\theta)=a_0+P^*\left(1-\frac{J_0\left(\frac{r}{R_0}\sqrt{Bo}\right)}{J_0\left(\sqrt{Bo}\right)}\right)+\sum_{n=1}^{\infty}\left(a_n\cos(n\theta)+b_n\sin(n\theta)\right)\frac{J_n\left(\frac{r}{R_0}\sqrt{Bo}\right)}{J_n\left(\sqrt{Bo}\right)},\quad(7)$$

where the constant $P^*(=Pd_c)$ can be calculated via the volume constraint (see Supplement 1 Section S1).

Figure 2(a) presents solutions of Eq. (7) for several Bond numbers and several values of n, representing bounding frame heights with a single azimuthal frequency. We note that in contrast to n, which are discrete, the Bond number is continuous, and the values presented here are a subset chosen to illustrate its qualitative effect on the resulting surface. These basic modes can be conveniently arranged in a pyramid structure in accordance with the wavenumber of the periodic boundary condition, with the outermost layer of the pyramid corresponding to neutral buoyancy conditions, i.e., $Bo=0$, and an increasing Bond number toward the center. Each layer in Fig. 2(a), corresponding to a fixed Bo number, represents a group of orthogonal surfaces that can be superposed to form a freeform surface, $h(r,\theta)=\sum_{n=0}^{\infty}h^{(n)}$, where

$$h^{(n)}=\begin{cases}\frac{a_n}{J_n(\sqrt{Bo})}J_n\left(\frac{r}{R_0}\sqrt{Bo}\right)\cos(n\theta)+\frac{b_n}{J_n(\sqrt{Bo})}J_n\left(\frac{r}{R_0}\sqrt{Bo}\right)\sin(n\theta), & n>0\\ a_0+P^*\left(1-\frac{J_0\left(\frac{r}{R_0}\sqrt{Bo}\right)}{J_0(\sqrt{Bo})}\right), & n=0\end{cases}.\quad(8)$$

We note that $h^{(0)}$ serves as a baseline surface on which the other modes are constructed and is also the only component in the solution that is a function of the injected volume. A particular case is that of $P^*=0$ (i.e., $V=\pi a_0 R_0^2$), in which the base term reduces to a constant, meaning that the base term does not contribute to optical power. For any other volume, the baseline solution represents a Bessel surface, which for the particular case of $Bo=0$ is a spherical lens. In Fig. 2(a) the baseline surface appears at the center column of the pyramid, representing the case of a homogenous boundary condition, corresponding to a cylindrical frame with a uniform height. For the case of $Bo=0$, the solution can be further simplified and represented conveniently using the power series (see Supplement 1 Section S2):

$$h(r,\theta)=a_0+2\left(\frac{V}{\pi R_0{}^2}-a_0\right)\left(1-\left(\frac{r}{R_0}\right)^2\right)+\sum_{n=1}^{\infty}\left(a_n\cos(n\theta)+b_n\sin(n\theta)\right)\left(\frac{r}{R_0}\right)^n.\quad(9)$$

This representation is also equivalent to representation by Zernike polynomials of the order $Z_n^{|m|=n}$ [32]. All other surfaces in the pyramid are not equivalent to Zernike polynomials, yet as Fig. 2(a) shows, have similar optical functionality.

Figure 2(b) shows that the extent to which the boundary shape affects the inner regions of the surface is a strong function of the wavenumber, n. As n increases, the influence of the boundary is increasingly more localized, as can also be seen by the r^n dependence in Eq. (9). This behavior holds also for other values of Bo. Clearly, the method cannot be used to create high-resolution features at the center of the component, but at the same time the solutions are insensitive to high-frequency deviations on the bounding frame (e.g., its surface roughness).

The Bond number represents the deviation from neutral buoyancy, and as shown in Fig. 2(c), tends to accentuate the effect of the bounding frame geometry. As the figure shows, increasing the Bond number can also invert the local curvature and create new local extrema. For a fixed Bond number, the injected volume can also have a significant effect on the shape of the resulting component, as illustrated by Fig. 2(d). By increasing the volume, the surface is transformed completely—from having a central valley with two side peaks to having a central peak with two side valleys. Combined, these three effects—the frame shape, the Bond number, and the volume, which are captured by Eq. (7)—provide significant degrees of freedom in the design of desired surfaces.

3. EXPERIMENTAL

Figure 3 illustrates the fabrication process of freeform surfaces using the fluidic shaping method. We use a 3D printer to print a rigid cylindrical bounding frame with a desired height variation along the azimuthal direction. We seal the bottom of the frame with a flat glass substrate and position it at the bottom of a larger container. We inject a desired volume of optical liquid into the frame and fill the container with immersion liquid until the frame is entirely submerged. Finally, we illuminate the container with UV light for several minutes to solidify the optical liquid. The optical component is then ready and can be removed from the immersion liquid. The bounding frame can be detached from the component and reused, or it can remain attached to it and serve as a mechanical interface.

Figure 4 presents the design and fabrication of a freeform optical component using the fluidic shaping method, and a

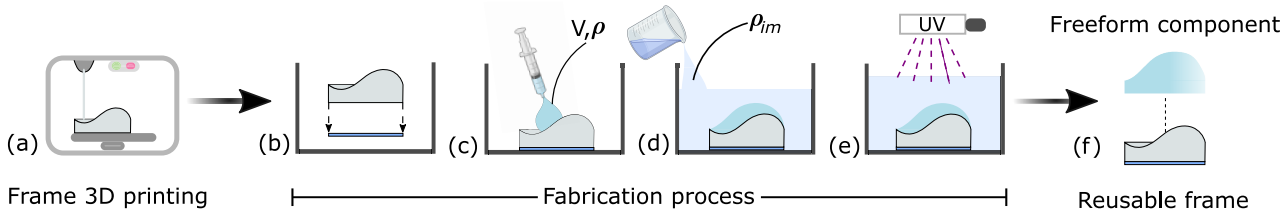

Fig. 3. Illustration of the workflow for the fabrication of freeform optical components using the fluidic shaping method. (a) A bounding frame with a desired azimuthal height variation is printed using a 3D printer. (b) The frame is sealed at its bottom using a flat window and positioned at the bottom of a larger container. (c) The inner part of the frame is filled with an optical liquid of volume V, according to its design. (d) The container is filled with an immersion liquid of a density ρ_{im} set by the desired Bond number. The immersion liquid volume is insignificant, as long as the frame and optical liquid are completely submerged. (e) The optical liquid is allowed to equilibrate and achieve its minimum energy state and is then illuminated with UV light to cure it. (f) The solid component can be removed from the immersion liquid. The frame and the immersion liquid can both be reused for the fabrication of additional components.

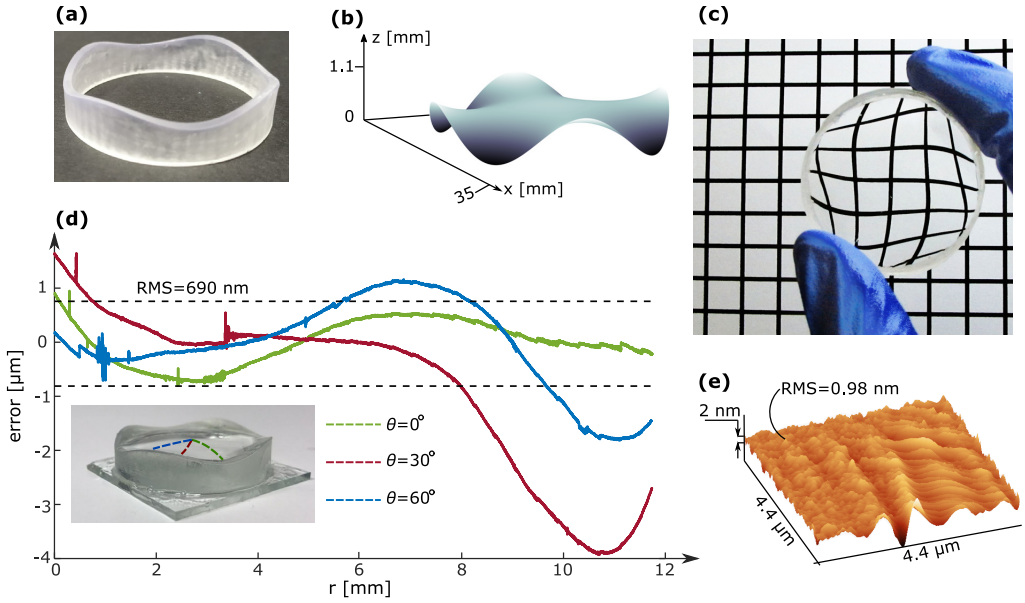

Fig. 4. Design, fabrication, and characterization of a freeform optical component. (a) Image of a 35 mm diameter 3D printed bounding frame with an azimuthal height variation of $h(R_0, \theta) = 0.55 \sin(4\theta)$ mm. (b) Image of the predicted 3D surface, based on Eq. (7), for an injected volume of $V = 3$ ml and a Bond number of $Bo = 3$. (c) Image of the resulting solidified component over graph paper. (d) Plot of the error between the measured optical surface and the theoretical surface for three cross sections 0°, 30°, 60°. The dashed line indicates the root-mean-square of the error for the three lines, RMS = 690 nm. See Dataset 1, Ref. [35] for underlying values. (e) An AFM measurement of surface roughness, showing an RMS of 0.98 nm.

comparison of its surface topography with the theoretical prediction. Figure 4(a) presents the frame providing the boundary conditions for fabricating the component, printed on a consumer-grade 3D printer. Figure 4(b) presents the expected resulting surface as obtained from Eq. (7) for a bounding frame with four sinusoidal periods, i.e., $h(R_0, \theta) = b_4 \sin(4\theta)$, where $b_4 = 0.55$ mm, $R_0 = 17.5$ mm, a Bond number of $Bo = 3$, and a volume of $V = 3$ mL. Figure 4(c) presents the resulting component after solidification. The entire fabrication process required 40 min to complete, of which 30 min were spent on 3D printing of the frame, and 10 min on manual injection of the liquids, curing, removal from the container, and drying. Using a digital holographic microscope (DHM R-1000 LynceeTec, Switzerland) we measured the topography of the resulting freeform surface along three radial lines (0°, 30°, 60°). A detailed description of the fabrication process and the measurement technique is available in Supplement 1 Sections S3 and S4.

Since our process is currently entirely manual, we expect inaccuracies in the injected volume and in the density of the immersion liquid. In addition, the shape of the boundary is affected by the ±25 μm accuracy of the 3D printer. Hence, we first turn to extract the global parameters—the Bond number, the injected volume, and the amplitude of the frame-height variation, from the resulting component. Using a least means squares fit between the three measured lines and the theoretical model, we obtain $Bo = 2.91$, $V = 3.21$ ml, $b_4 = 0.56$ mm, which are well within the expected error of our manual process.

Figure 4(d) presents the difference between the measured surface height along the three radial lines, and the theoretical values along these lines using the extracted parameters. The results show that for radii smaller than 8 mm the differences between theory and measurements are capped at approximately 1 μm and grow to 4 μm toward the edges of the frame. The RMS of the error, over all three lines, is 690 nm. Figure 4(e) presents the measurement of the surface roughness of the resulting component over an area of 4.4×4.4 μm, using atomic force microscopy (AFM), showing an RMS value of 0.98 nm, as expected due to the smoothness of the liquid–liquid interface.

4. DISCUSSION

We introduced a new method for the design and fabrication of freeform components based on shaping of fluidic interfaces. We showed that the steady-state topography of the liquid interface is dictated by the shape of a bounding frame, the volume of the optical liquid, and the dimensionless Bond number. The fabrication time, dominated by the 3D printing of the frame, is of the order of tens of minutes and is independent of the complexity of the frame shape. Owing to the natural smoothness of liquid–liquid interfaces, the resulting surface roughness is of the order of 1 nm without the need for any post-polishing steps. In addition, while the results presented in this work were obtained using a specific polymer, in principle, any curable liquid can be used to form a freeform component, provided that an appropriate immersion liquid can be identified. We have successfully implemented the method using silicone oils and a variety of optical adhesives having different optical and mechanical properties.

The range of surfaces that can be produced using the method can be described by summation of any number of Fourier–Bessel modes that share a single Bond number. Additional degrees of freedom can be gained by utilizing frames that vary azimuthally on both ends. The optical liquid injected into the frame would thus have two contact surfaces with the immersion liquid, creating components with freeform surfaces on both sides. Moreover, enclosing each end of the frame within a different immersion liquid would result in surfaces that are based on different Bond numbers, allowing to further increase the degrees of freedom of the component.

Finally, while our work here focused on fabrication of solidified components, the optical fluid may purposely remain in its fluidic state, allowing the implementation of dynamically controlled optical components. Simple real-time changes may be possible by injecting or aspirating optical liquid, or by adjusting the immersion liquid density. A higher level of control could perhaps be achieved by implementing a deformable bounding frame whose shape can be modified in time.

Funding. European Research Council (678734).

Acknowledgment. This project has received funding from the European Research Council under the European Union's Horizon 2020 Research and Innovation Programme, grant agreement 678734 (MetamorphChip). We thank Baruch Rofman for performing the AFM surface quality measurements, and Rishabh Das for critically reviewing an earlier version of the derivation.

Disclosures. The authors declare no conflicts of interest.

Data Availability. Data underlying the results presented in this paper are available in Dataset 1, Ref. [35].

Supplemental document. See Supplement 1 for supporting content.

[†]These authors contributed equally to this paper.

REFERENCES

1. J. P. Rolland, M. A. Davies, T. J. Suleski, C. Evans, A. Bauer, J. C. Lambropoulos, and K. Falaggis, "Freeform optics for imaging," Optica **8**, 161–176 (2021).
2. F. Z. Fang, X. D. Zhang, A. Weckenmann, G. X. Zhang, and C. Evans, "Manufacturing and measurement of freeform optics," CIRP Ann. **62**, 823–846 (2013).
3. J. Reimers, A. Bauer, K. P. Thompson, and J. P. Rolland, "Freeform spectrometer enabling increased compactness," Light Sci. Appl. **6**, e17026 (2017).
4. K. Takahashi, "Development of ultrawide-angle compact camera using free-form optics," Opt. Rev. **18**, 55–59 (2011).
5. E. R. Dowski and W. T. Cathey, "Extended depth of field through wavefront coding," Appl. Opt. **34**, 1859–1866 (1995).
6. Y. Wang, Z. Li, X. Liu, F. Fang, and X. Zhang, "Freeform-objective Chernin multipass cell: application of a freeform surface on assembly simplification," Appl. Opt. **56**, 8541–8546 (2017).
7. J. Ye, L. Chen, X. Li, Q. Yuan, and Z. Gao, "Review of optical freeform surface representation technique and its application," Opt. Eng. **56**, 110901 (2017).
8. A. Cao, J. Wang, H. Pang, M. Zhang, L. Shi, Q. Deng, and S. Hu, "Design and fabrication of a multifocal bionic compound eye for imaging," Bioinspir. Biomim. **13**, 026012 (2018).
9. W. Jia, B. Zhang, and S. Li, "Progressive multifocal liquid lenses based on asymmetric freeform surface structure of nonuniform thickness elastic membranes with different constraints," Int. J. Opt. **2019**, 1–12 (2019).
10. B. V. Rao, K. V. Sriram, and C. S. Narayanamurthy, "Design of two-mirror telescope systems with freeform surfaces: modified configurations and analysis," Proc. SPIE **7**, 014002 (2021).
11. N. Bregenzer, M. Bawart, and S. Bernet, "Zoom system by rotation of toroidal lenses," Opt. Express **28**, 3258–3269 (2020).
12. S. Bernet, "Zoomable telescope by rotation of toroidal lenses," Appl. Opt. **57**, 8087–8095 (2018).
13. Z. Feng, L. Huang, M. Gong, and G. Jin, "Beam shaping system design using double freeform," Opt. Express **21**, 14728–14735 (2013).
14. B. Yang, K. Lu, W. Zhang, and F. Dai, "Design of a free-form lens system for short distance projection," Proc. SPIE **8128**, 81280E (2011).

15. Z. Zhuang, Y. Chen, F. Yu, and X. Sun, "Field curvature correction method for ultrashort throw ratio projection optics design using an odd polynomial mirror surface," Appl. Opt. **53**, E69–E76 (2014).
16. T. Ma, J. Yu, P. Liang, and C. Wang, "Design of a freeform varifocal panoramic optical system with specified annular center of field of view," Opt. Express **19**, 3843–3853 (2011).
17. P. Zamora, A. Cvetkovic, M. Buljan, M. Hernández, P. Benítez, J. C. Miñano, O. Dross, R. Alvarez, and A. Santamaría, "Advanced PV concentrators," in *34th IEEE Photovoltaic Specialists Conference (PVSC)* (2009).
18. R. Wu, H. Li, Z. Zheng, and X. Liu, "Freeform lens arrays for off-axis illumination in an optical lithography system," Appl. Opt. **50**, 725–732 (2011).
19. F. Fang, N. Zhang, and X. Zhang, "Precision injection molding of freeform optics," Adv. Opt. Technol. **5**, 305–309 (2016).
20. M. Roeder, T. Guenther, and A. Zimmermann, "Review on fabrication technologies for optical mold inserts," Micromachines **10**, 233 (2019).
21. L. Zhu, Z. Li, F. Fang, S. Huang, and X. Zhang, "Review on fast tool servo machining of optical freeform surfaces," Int. J. Adv. Manuf. Technol. **95**, 2071–2092 (2018).
22. Z. Xia, F. Fang, E. Ahearne, and M. Tao, "Advances in polishing of optical freeform surfaces: a review," J. Mater. Process. Technol. **286**, 116828 (2020).
23. V. Mishra, D. Sabui, D. R. Burada, V. Karar, S. Jha, and G. S. Khan, "Experimental investigations on slow tool servo process parameters for freeform optics machining," Mater. Manuf. Process. **35**, 797–810 (2020).
24. H. Feng, R. Xia, Y. Li, J. Chen, Y. Yuan, D. Zhu, S. Chen, and H. Chen, "Fabrication of freeform progressive addition lenses using a self-developed long stroke fast tool servo," Int. J. Adv. Manuf. Technol. **91**, 3799–3806 (2017).
25. G. Shao, R. Hai, and C. Sun, "3D printing customized optical lens in minutes," Adv. Opt. Mater. **8**, 1901646 (2020).
26. R. Kirchner and H. Schift, "Thermal reflow of polymers for innovative and smart 3D structures: a review," Mater. Sci. Semicond. Process. **92**, 58–72 (2019).
27. Z. Hong and R. Liang, "IR-laser assisted additive freeform optics manufacturing," Sci. Rep. **7**, 7145 (2017).
28. B. G. Assefa, T. Saastamoinen, J. Biskop, M. Kuittinen, J. Turunen, and J. Saarinen, "3D printed plano-freeform optics for non-coherent discontinuous beam shaping," Opt. Rev. **25**, 456–462 (2018).
29. F. Kotz, A. S. Quick, P. Risch, T. Martin, T. Hoose, M. Thiel, D. Helmer, and B. E. Rapp, "Two-photon polymerization of nanocomposites for the fabrication of transparent fused silica glass microstructures," Adv. Mater. **33**, 2006341 (2021).
30. T. Gissibl, S. Thiele, A. Herkommer, and H. Giessen, "Two-photon direct laser writing of ultracompact multi-lens objectives," Nat. Photonics **10**, 554–560 (2016).
31. V. Frumkin and M. Bercovici, "Fluidic shaping of optical components," Flow **1**, E2 (2021).
32. V. Lakshminarayanan and A. Fleck, "Zernike polynomials: a guide," J. Mod. Opt. **58**, 545–561 (2011).
33. M. Gelfand and S. V. Fomin, *Calculus of Variations* (Prentice-Hall, 1963).
34. A. D. Polyanin and V. E. Nazaikinskii, *Handbook of Linear Partial Differential Equations* (Taylor and Francis, 2016).
35. M. Elgarisi, V. Frumkin, O. Luria, and M. Bercovici, "Measurements of the freeform surface (R_0=17.5 mm, b_4=0.56 mm, V=3.21 mL, Bo=2.91, phi_0=21.45 deg), and its difference from the theoretical surface," figshare (2021) https://doi.org/10.6084/m9.figshare.16713010.